POLYMER
TESTING

materialstoday

Classifying condition of ultra-high-molecular-weight polyethylene ropes with wide-angle X-ray scattering

Aksel S. Obdrup [a], D.C. Florian Wieland [b], Mathias K. Huss-Hansen [a,c], Matthias M.L. Arras [d,e,*], Matti Knaapila [a,f]

[a] Department of Physics, Technical University of Denmark, 2800, Kongens Lyngby, Denmark
[b] Institute for Metallic Biomaterials, Helmholtz Zentrum Hereon, Max–Planck Strasse 1, 21502, Geesthacht, Germany
[c] NanoSYD, Mads Clausen Institute, University of Southern Denmark, Alison 2, 6400, Sønderborg, Denmark
[d] Royal DSM, DSM Materials Science Center, Urmonderbaan 22, 6167 RD, Geleen, The Netherlands
[e] DSM Protective Materials B.V., Urmonderbaan 22, 6167 RD, Geleen, The Netherlands
[f] Department of Physics, Norwegian University of Science and Technology, Høgskoleringen 5, 7491, Trondheim, Norway

ARTICLE INFO

ABSTRACT

Ropes of ultra-high-molecular-weight polyethylene (UHMWPE) are replacing steel wires in many applications and nondestructive testing to monitor their condition is of scientific and commercial interest. In this work, wide-angle X-ray scattering (WAXS) combined with linear discriminant analysis (LDA) is proposed as classification method to distinguish between healthy and damaged UHMWPE ropes. Healthy (as produced, after pre-stretching) and damaged (in-field use) ropes ($\varnothing = 22\,mm$) have been analyzed using synchrotron radiation. Firstly, it is demonstrated that scans of healthy and damaged ropes can be distinguished with 100% cross-validated test classification accuracy using LDA; this is shown both with the input data consisting of pre-processed 1D WAXS data and with physical parameters retrieved by fitting the WAXS data. Secondly, it is demonstrated that the classification performance is similar using the two forms of input data and that the noise could be increased by a factor of three while maintaining 100% test classification accuracy across all the three cross-validation folds.

1. Introduction

Polyethylene (PE) is among the most widely used polymers and has a simple structure consisting of a backbone of carbon atoms each having two attached hydrogen atoms. Ultra-high-molecular-weight polyethylene (UHMWPE) has a number average molecular weight between 10^6–$10^7\,g\,mol^{-1}$. In the late 1970's and in the beginning of the 1980's Smith, Leemstra and co-workers from the central laboratory of DSM established the production of UHMWPE filaments via gel-spinning [1–6]. This process was patented by DSM and commercialized under the tradename of Dyneema® and so produced fibers have strength and modulus of up to $4\,GPa$ and $154\,GPa$ which is comparable to steel wires ($2\,GPa$ and $184\,GPa$).

UHMWPE ropes are emerging as a safe, strong and light-weight alternative to steel wires in many areas such as heavy lifting, maritime applications, commercial fishing, aquaculture, wind, land cranes and deep sea operations [7,8]. In these industries, the condition of ropes and wires are regularly monitored to ensure safe operations. For steel wires, this is typically done using magnetic flux leakage techniques [9].

UHMWPE ropes can also be subject to various damage mechanisms, such as abrasion, creep, tensile fatigue and heating, which are critical to detect. The International Organization for Standardization ISO and the maritime classification society Det Norske Veritas DNV define standards for off-shore fiber ropes describing current monitoring methods based on visual inspections and counting of loading cycles [10,11]. Visual inspection is, however, only indirectly sensitive to microscopic defects and internal abrasion is not visible.

There is a demand for more quantitative non-destructive testing (NDT) methods to monitor the condition of UHMWPE ropes. In 2017, Schlanbusch et al. [12] reviewed existing literature and patents on condition monitoring methods for synthetic fiber ropes. They describe two distinct classification families (direct/indirect). The first family comprises of directly measuring physical quantities of the rope including methods like thermography, diameter measurements and acoustic emission. The second family focusses on embedding additional materials into the ropes as indicators/sensors. The embedding methods are based on incorporating strength members that are visible by either

---

* Corresponding author.
  E-mail addresses: aksel.obdrup@fysik.dtu.dk (A.S. Obdrup), matthias.arras@dsm.com (M.M.L. Arras), matti.knaapila@ntnu.no (M. Knaapila).
  URL: http://www.dyneema.com (M.M.L. Arras).

X-ray imaging or magnetism. According to these authors, no single existing measurement will be sufficient to cover all different failure modes.

The unit cell of polyethylene and its dimensions were described by Bunn [13] using X-ray crystallography. The unit cell was identified as orthorhombic. Seto et al. [14] studied deformation processes of oriented polyethylene with X-rays. They identified extra Bragg reflections of compressed polyethylene as originating from a new monoclinic crystal structure. Russell et al. [15] studied the monoclinic modification by battering samples with the orthorhombic structure beyond the yield point. The monoclinic phase was identified with wide-angle X-ray scattering (WAXS) and nuclear magnetic resonance (NMR) spectroscopy. The fraction of the monoclinic phase was typically below 10%. In most cases the authors observed only the most dominant 001 monoclinic peak at $Q = 13.7\,\mathrm{nm}^{-1}$, due to the next two monoclinic peaks overlapping with the orthorhombic 200 peak.

Collins and Dalton [16,17] studied the crystal morphology of UHMWPE samples under tensile strain by a combination of *in-situ* WAXS and small-angle X-ray scattering (SAXS) allowing them to probe both the crystalline structure and the higher level shish-kebab morphology. SAXS data showed that the lamella thicknesses are constant at low strain and then start to increase up to a strain of 0.2. This crystal perfection process is also associated with a martensitic orthorhombic to monoclinic phase transition within the crystal regions observed by WAXS.

Balzano et al. [18] proposed a multiscale model to describe the molecular structure of Dyneema® fibers from the length scales of the unit cell up to the filament level in static and dynamic conditions. *In-situ* WAXS was performed under tensile testing. Their first observation was that the azimuthal width of the Bragg peaks did not change with strain. The authors analyzed equatorial intensity profiles and observed significant evolution of the peak width and center position for the orthorhombic 110 and 200 peak. At low strains both peaks shift towards a larger momentum transfer Q which indicates, with the onset of plastic deformation, a compression of the orthorhombic unit cell along the *a*- and *b*-axis. At larger strains the 200 peak position continues to increase monotonically while the 110 peak position begins to move towards smaller Q values, which indicates that while the contraction continues along the *a*-axis the orthorhombic unit cell will begin to expand along the *b*-axis.

Istrate et al. [19] studied UHMWPE ropes with wear history by differential scanning calorimetry (DSC) and fast scanning calorimetry. These authors have shown how melting endotherms are affected by wear: increase in rope wear, pushes the (deconvoluted) endotherm peak to higher temperatures. But more importantly, an increase in a low-melting fraction was detected which has been attributed to a change in crystal morphology, namely chain folded crystals.

It is thus apparent that there are correlations between morphology and wear history of UHMWPE fibers. However, in previous literature focus has been on filaments and no quantitative models linking the crystalline morphology to the mechanical properties of entire ropes have been provided.

In recent years the ability to capture, store and process large quantities of data has been greatly enhanced. This has lead to a rapid growth of data driven processes and modeling in many fields including automatic detection of material degradation. Machine learning algorithms have for example surpassed visual inspection by humans for the detection of metal corrosion and cracks in concrete constructions [20,21]. These algorithms are based on analyzing pictures of the material with models trained on libraries of previously seen and labeled data, also known as supervised learning.

Doaei et al. [22] used thermal pulsing and IR thermography combined with machine learning to classify faults for electrofusion polyethylene joints used in gas pipelines. As expected, they found that the overall test classification accuracy increased with size of the data set. In their study, logistic regression with elastic net regularization showed

better test classification accuracy than random decision forests and k-means clustering.

Hiles et al. [23] published a study where formulations of cross-linked polyethylene pipes were classified by applying machine learning concepts to infrared spectra. Their goal was to understand how the pipe formulation affected performance. By applying principle component analysis (PCA) and supervised classification methods, the authors show that IR absorbance peaks could be used to determine the formulations of the pipes with very high accuracy.

Falconer et al. [24], applied machine-learning algorithms to optical and thermal image data for Dyneema fiber rope condition monitoring during continuous bending over sheaves with very promising for remaining useful life prediction. Their data was based on information obtained from the surface of the rope.

A common linear method used for classification tasks is linear discriminant analysis (LDA). This method has been applied to attenuated total reflectance Fourier transform infrared (ATR-FTIR) microspectroscopy data to diagnose colon cancer with an accuracy of 95.8% between cancer and normal tissue classes on a test set [25]. The same authors also used LDA on infrared spectrometry data of diesel samples for quality screening purposes [26]. The trained model had an accuracy of 95.6% between samples that passed/failed the quality control on a test set.

Elsewhere, LDA has also been used to discriminate between nine differently branded polyethylene films with 100% accuracy based on ATR-FTIR spectroscopy data [27], to discriminate between flavonoids with a sensor array of five fluorescent polymers with 100% accuracy [28] or to discriminate between carbohydrates with supramolecular sensing [29].

In this paper, we propose a condition monitoring method for UHMWPE ropes based on combining WAXS measurements with supervised learning. WAXS is employed as NDT method which primarily probes the crystalline phase of the material and such measurements of UHMWPE ropes have been performed. Predictive models of rope condition have been trained using LDA as a supervised learning technique.

2. Experimental procedures and data pre-processing

The studied 22 mm thick ropes of Dyneema® SK78 fibers were manufactured and provided for this experiment by Dynamica Ropes ApS: A healthy rope and a damaged rope. The healthy rope has only been subject to pre-stretching to remove the constructional elongation. The damaged rope has been subject to pre-stretching plus internal and external abrasion and has been retired from commercial use by a customer of Dynamica Ropes ApS.

WAXS measurements were carried out at the High Energy Materials Science Beamline (HEMS) at PETRA III, DESY, Hamburg. The wavelength used was 0.014 05 nm. A CdTe Pilatus 2M detector was used and placed at a distance of 2.243 m allowing us to probe the Q-range above 12.5 nm^{-1}. The size of the X-ray beam was 100 μm × 100 μm. The complete ropes were placed on a motorized stage and, aiming for the center, they were scanned in a linear fashion along the rope direction in steps of 300 μm with an exposure time of 10 s per scan. In total 70 scans were performed for each rope. Each observation was corrected for differences in transmission. The transmission signal was recorded via a semi transparent beamstop directly on the Pilatus detector.

The data was masked and azimuthally integrated to 500 linearly spaced points in the Q-range from 12.5 to 22.5 nm^{-1} with the pyFAI library [30]. Furthermore, the data was normalized to sum to 1 to account for differences in scattering volume effects.

Fig. 1 plots the mean WAXS curves calculated from all scans for the healthy and damaged ropes on a logarithmic scale in green and red, respectively. Standard deviations are indicated by shaded areas. The monoclinic and orthorhombic peaks are indicated with cyan and purple background, respectively.
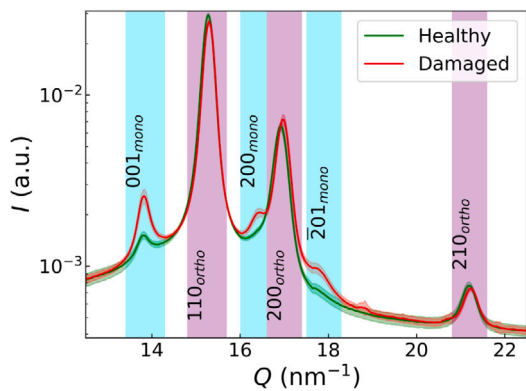
Fig. 1. Mean WAXS curves calculated from 70 scans of a healthy (green) and 70 scans of a damaged rope (red). Standard deviations are indicated by shaded areas. (For interpretation of the references to color in this figure legend, the reader is referred to the web version of this article.)
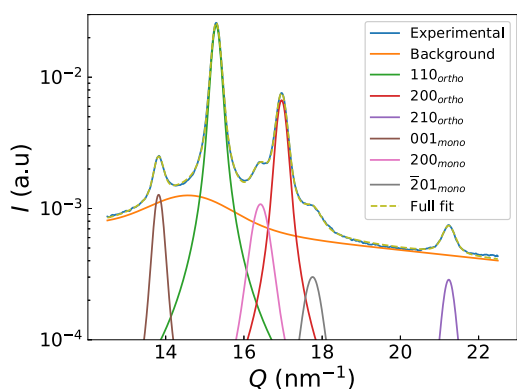
Fig. 2. Fit of a representative azimuthally integrated WAXS scan of the damaged rope to deconvolute the pattern into individual peaks.

Fig. 3. Box plots of fitted values for crystalline fractions of scans from the healthy (green) and damaged rope (red). (For interpretation of the references to color in this figure legend, the reader is referred to the web version of this article.)

Fig. 4. Box plots of fitted values for unit cell parameters of scans from the healthy (green) and damaged rope (red). (For interpretation of the references to color in this figure legend, the reader is referred to the web version of this article.)

The WAXS curves have also been processed in terms of fitting with the aim of deconvoluting each measurement to fewer and less correlated variables. This was done using the lmfit library [31]. For each of the 140 observations each Bragg feature was fitted by a Pseudo-Voigt function and the amorphous background was fitted by a combination of a Pseudo-Voigt and a linear function.
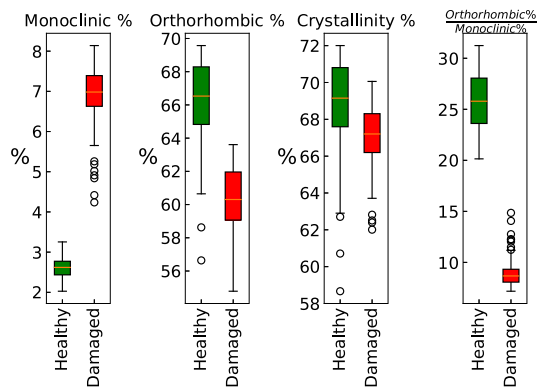
Fig. 2 shows the fit/deconvolution for a single representative WAXS curve obtained from the damaged rope. The overall experimental curve is captured accurately by the full fit. The χ^2-residuals are below 10^{-5} for all 140 observations and thus all fits are deemed acceptable for further analysis.

The fitted amplitudes were used to calculate the fraction of material in monoclinic and orthorhombic crystalline phase and the overall crystallinity. The fractions of material in crystalline phase C was estimated by the integrated intensity of the WAXS curve from the crystalline peaks I_C divided by the total intensity I integrated:
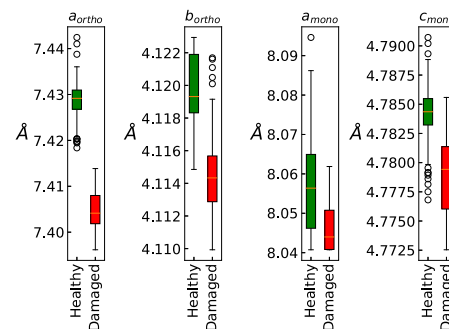
$$X_C\,[\%] = \frac{\int_{Q_{\min}}^{Q_{\max}} I_C \, \mathrm{d}Q}{\int_{Q_{\min}}^{Q_{\max}} I \, \mathrm{d}Q} \times 100. \qquad (1)$$

Analogously, the monoclinic or orthorhombic crystal fraction/content can be caluclated by substituting I_C for I_C^{mono} or for I_C^{ortho} in the above equation.

Overall crystallinity, monoclinic content, orthorhombic content and lastly the fraction between orthorhombic and monoclinic content were chosen as input variables for the LDA analysis. Box plots of estimated values for each of the 70 scans for each of the two ropes are shown in Fig. 3. The bottom and top of each box represents the 25th and 75th

percentile while the yellow line indicates the median (50th percentile). The length of the whiskers on the boxes are calculated by multiplying the interquartile range, i.e. from the 25th to the 75th percentile, by 1.5. However if the maximum/ minimum value is within this range then the whisker is set at the maximum/minimum. If observations fall outside the whiskers they are marked as potential outliers with open circles. Scans containing potential outliers were investigated individually but none were deemed unfit for purpose and all were included in the dataset presented below.

The peak positions $\mathbf{Q}_{hkl}$ were used to estimate unit cell parameters. This was done using the following relations between peak position, Miller indices and unit cell parameters:

For the orthorhombic unit cell the relation reads:

$$\frac{2\pi}{\left|\mathbf{Q}_{hkl}^{\mathrm{ortho}}\right|} = \frac{1}{\sqrt{\dfrac{h^2}{\left|\mathbf{a}_{\mathrm{ortho}}\right|^2} + \dfrac{k^2}{\left|\mathbf{b}_{\mathrm{ortho}}\right|^2} + \dfrac{l^2}{\left|\mathbf{c}_{\mathrm{ortho}}\right|^2}}}. \qquad (2)$$

The relation for the monoclinic unit cell is:

$$\frac{2\pi}{\left|\mathbf{Q}_{hkl}^{\mathrm{mono}}\right|} = \frac{\sin\beta}{\sqrt{\dfrac{h^2}{\left|\mathbf{a}_{\mathrm{mono}}\right|^2} + \dfrac{k^2 \sin^2\beta}{\left|\mathbf{b}_{\mathrm{mono}}\right|^2} + \dfrac{l^2}{\left|\mathbf{c}_{\mathrm{mono}}\right|^2} - \dfrac{2hl\cos\beta}{\left|\mathbf{a}_{\mathrm{mono}}\right|\left|\mathbf{c}_{\mathrm{mono}}\right|}}}, \qquad (3)$$

with $\beta = 107.9^\circ$ for polyethylene. Input variables, both a_{ortho} and b_{ortho}, were estimated from the orthorhombic 200 and 110 peaks, respectively. Furthermore a_{mono} and c_{mono} were estimated from the monoclinic 200 and 001 peaks, respectively. Box plots of estimated values for each of the 70 scans for each of the two ropes are shown in Fig. 4.

The full width at half maximum (FWHM) of the peaks were used to estimate mean sizes of crystalline domains τ_{hkl} perpendicular to a set of hkl planes. These mean sizes are estimated by the Scherrer equation:
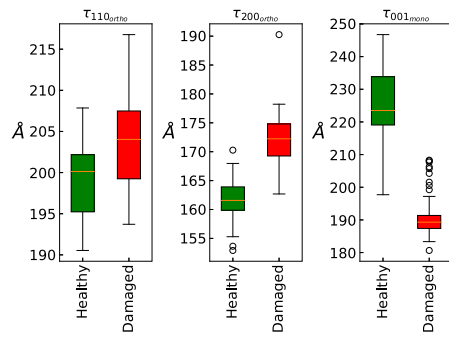
Fig. 5. Box plots of fitted values for mean sizes of crystalline domains from the healthy and damaged rope.

Fig. 6. Linear discriminant from first cross-validation fold between scans from healthy and damaged rope with 1D WAXS input data.

$$\tau_{hkl} = \frac{2K\pi}{\Delta Q_{hkl}}, \qquad (4)$$

where K is the shape factor which in this work is set to 0.9 corresponding to a symmetric crystallite and ΔQ_{hkl} is the FWHM of the hkl reflection.

The most significant Bragg features $\tau_{o_{110}}$, $\tau_{o_{200}}$ and $\tau_{m_{001}}$ were chosen as input variables. Box plots of estimated values for each of the 70 scans for each of the two ropes are shown in Fig. 5.

3. Linear discriminant analysis

LDA is a commonly used method to determine linear combinations of features which separate classes of data both for the purpose of visualization and for classification [32]. LDA projects the data $\mathbf{X}$ onto a C-1 dimensional sub-space, where C is the number of classes, while maximizing the ratio of between-class variance and within-class variance. With two classes this sub-space will thus be spanned by a single linear discriminant $\mathbf{w}$ which is determined in the following way.

When data of two classes (class 0 and 1) with means μ_0, μ_1 and covariance matrices $\sum_0$, $\sum_0$ are projected onto a vector $\mathbf{w}$ this will result in new class means $\mathbf{w} \cdot \mu_0$, $\mathbf{w} \cdot \mu_1$ and variances $\mathbf{w}^T \sum_0 \mathbf{w}$, $\mathbf{w}^T \sum_1 \mathbf{w}$. Fisher [33] defined the ratio between-class variance and within-class variance by:

$$\frac{\sigma_{\text{between}}^2}{\sigma_{\text{within}}^2} = \frac{\left(\mathbf{w} \cdot \mu_0 - \mathbf{w} \cdot \mu_1\right)^2}{\mathbf{w}^T \sum_0 \mathbf{w} + \mathbf{w}^T \sum_1 \mathbf{w}}. \qquad (5)$$

This ratio is maximized when w is proportional to:

$$\mathbf{w} \propto \left(\sum\nolimits_0 + \sum\nolimits_1\right)^{-1} \left(\mu_1 - \mu_0\right). \qquad (6)$$

LDA makes the assumption that the covariances for the two classes are equal ($\sum = \sum_0 = \sum_1$).

Typically these means and covariances are not known and have to be estimated with a training set using maximum likelihood estimators. However when the number of training observations is small compared to the number of features the maximum likelihood estimator of the covariance matrix is unstable. To stabilize the estimator, one usually introduces a shrinkage parameter $\gamma \in [0, 1]$ which shrinks the estimate of the covariance matrix towards diagonal matrix of variances:

$$\hat{\sum} (\gamma) = (1 - \gamma) \hat{\sum} + \gamma \hat{\sigma}^2 \mathbf{I}. \qquad (7)$$

Typically one uses a larger shrinkage parameter when less training data is available compared to the number of predictors. The value of the shrinkage parameter is often determined by the lemma introduced by Ledoit and Wolf [34].

After projection the data is discriminated by a threshold c, typically set at the center between the two class means:

$$c = \mathbf{w} \cdot \left(\mu_0 + \mu_1\right). \qquad (8)$$
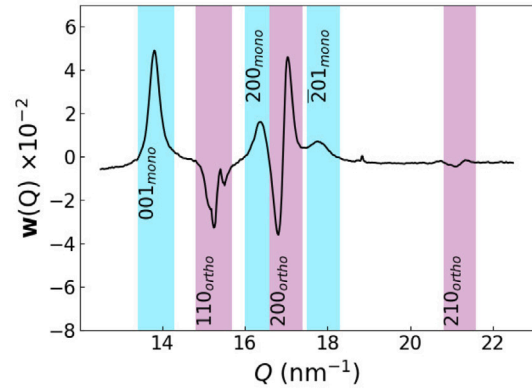
In this work, LDA has been performed with the scikit-learn library [35]. Stratified three-fold cross-validation has been performed, which ensures that both the training and test sets have equal fractions of observations from the healthy and damaged class. 2/3 of the data is stochastically selected for training (i.e. calculating $\mathbf{w}$ and c). The remaining 1/3 of the data is then used for independent testing, by applying the LDA classification process to these observations. The model is then evaluated by the test classification accuracy which is given by the percentage of correctly classified observations in the test set:

$$\text{Accuracy}[\%] = \frac{N_{\text{test}} - \sum_{i=1}^{N_{\text{test}}} \left| y_i - y_i^{\text{est}} \right|}{N_{\text{test}}} \times 100, \qquad (9)$$

where N_{test} is the number of observations in the test set, y_i is the true condition of observation i and y_i^{est} is the estimated condition by the model (0 if damaged and 1 if healthy).

3.1. LDA with 1D WAXS input data

Firstly, LDA was performed using the 1D WAXS data as input after normalization and centering by subtracting mean values for each Q-position. The shrinkage parameter was set to $\gamma = 0.5$, which is relatively large due to the large number of predictors with respect to the number of training observations.

The linear discriminant $\mathbf{w}$ is calculated using the training observations and Eq. (7). Fig. 6 shows the linear discriminant coefficients from the first cross-validation fold. The areas corresponding to monoclinic and orthorhombic peaks are indicated with cyan and purple background, respectively. The higher the absolute value of a coefficient the higher the importance of the scattering signal at that Q-value in terms of distinguishing between healthy and damaged ropes. These coefficients are very similar across all three cross-validation folds.

Fig. 7 shows projections of training and test data onto the linear discriminant $\mathbf{w}$. Each point represents a WAXS curve. The decision boundary is calculated using Eq. (8) and is illustrated by the background color indicating the class predicted of observations in each of the regions. LDA is able to classify all observations in the training set correctly. Furthermore, the classifier is shown to generalize well to data which has not been used for building the model, since all observations in the test set are classified correctly. The test classification accuracies across all three cross-validation folds were 100%.

3.2. LDA with fitted input data

Secondly, LDA was performed on fitted parameters obtained from deconvoluting the 1D scattering. The data was standardized by subtracting the mean and dividing by the standard deviation for each
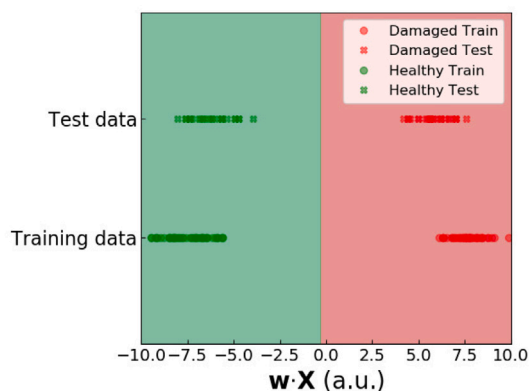
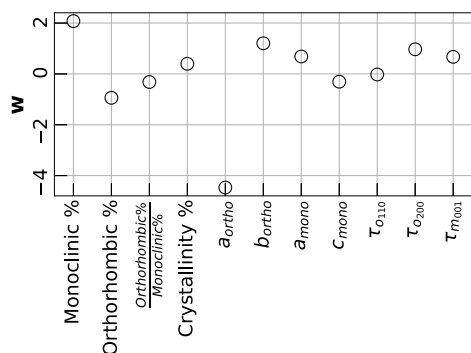**Fig. 7.** Projections of training and test 1D WAXS data onto the linear discriminant shown in Fig. 6.

Fig. 8. Linear discriminant from first cross-validation fold between scans from healthy and damaged rope with fitted input data.

Fig. 9. Projections of fitted training and test data onto the linear discriminant shown in Fig. 8.

Fig. 10. Test classification accuracy of LDA for 1D WAXS and fitted input data against noise level in the data (defined by the in-class standard deviations).

input parameter. The shrinkage parameter was set to $\gamma = 0.1$, which is significantly smaller than with the 1D WAXS input data due to the smaller number of predictors after the fitting procedure.

The linear discriminant is calculated using the training observations and Eq. (7). Fig. 8 shows the linear discriminant **w** from the first cross-validation fold. The linear discriminants from the two other folds are very similar.

Fig. 9 shows projections onto the linear discriminant of both training and test data. The decision boundary is again calculated using Eq. (8) and is illustrated by the background color indicating the class predicted of observations in each of the regions. LDA is able to classify all observations in both the training set and the test set correctly. The test classification accuracies across all three cross-validation folds were 100% which demonstrates that this predictive method based on fitted input parameters also generalizes to independent data.

4. Classification with simulated noise

From a practical point of view it is interesting to explore how this classification method responds to increased noise levels since it is likely that data will have a lower signal-to-noise ratio than the data presented in this work in a practical NDT setting. Therefore we have studied how the test classification accuracy is influenced when Gaussian noise is artificially added to the data set.

The level of noise is defined by the within-class standard deviations at each Q-position as shown by the shaded areas in Fig. 1. Noise has been added by simulating random Gaussian numbers with standard deviations of integer values (1–9) times the within-class standard deviations.
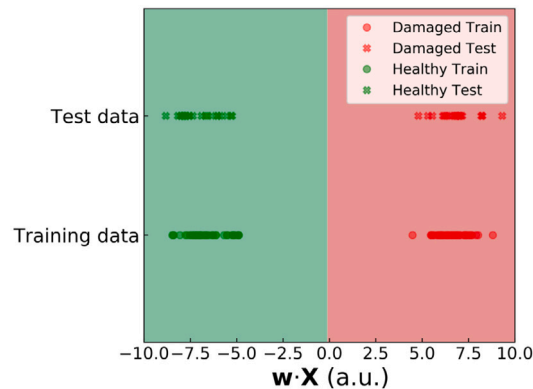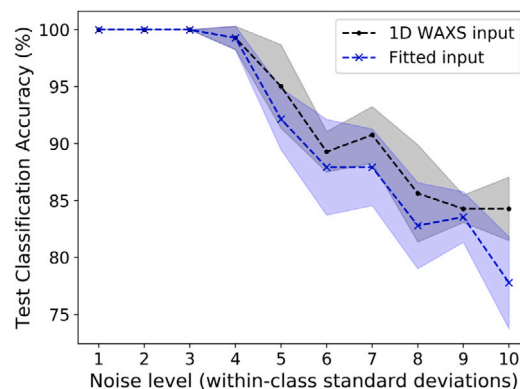
For each of the 10 new data sets with varying amounts of noise, including the original data set, three-fold cross-validation has been performed using LDA as a classifier with various signal-to-noise ratios.

As part of the pre-processing of the data a Savitzky–Golay filter of 1st order using 9 points was applied to smoothen the data [36]. This filter is applied before the fitting procedure.

The resulting mean test classification accuracies using either the 1D WAXS data or fitted parameters with various amounts of noise can be seen in Fig. 10. The shrinkage parameter is chosen by the Ledoit–Wolf lemma. The standard deviations are indicated by shaded areas and are estimated by the standard deviations of the test classification accuracies over the three cross-validation folds.

5. Discussion

Here, we monitored new and damaged 22 mm thick UHMWPE ropes using WAXS. For each rope 70 scans were measured and the pre-processed data analyzed using LDA. By use of three-fold cross-validation we demonstrate that LDA can separate the two classes of scans with 100% test accuracy; both when the input data was 1D WAXS or when physical parameters estimated obtained by peak deconvolution were used. Thus we show that wear induced changes in crystalline morphology of macroscopic UHMWPE ropes can be measured ex situ with WAXS and that this can be used as a probe for condition monitoring of UHMWPE ropes. From the presented and additional measurements (not shown), we know that the wear induced damage is not always homogeneously distributed across the cross-section of the rope. Nevertheless, this seems to be not an issue as far as binary classification is concerned.

We also illustrate how the trained models distinguish between WAXS scans of the healthy and damaged rope using 1D WAXS data and fitted parameters respectively in Figs. 6 and 8. The linear discriminant in Fig. 6 has positive values for all Q-values corresponding to monoclinic peaks. Projections onto this discriminant gives positive values for the damaged scans and negative values for the healthy scans. As easily understood, the transformation of orthorhombic to monoclinic phase is correlates with a damaged rope. Since the orthorhombic peaks are still dominant even in damaged ropes, in these cases the shifts of the peaks are more important. The linear discriminant shows either a minimum or the transition from peak to valley at the original location of the peak. For the 200 peak any shift towards higher Q (up until about $17.5\,\text{nm}^{-1}$) is associated with damage. This is consistent with existing literature on single UHMWPE filaments reporting an increase of monoclinic content with strain [16] and a contraction of the orthorhombic unit along the a-axis [18]. The linear discriminant is even easier to interpret once the scattering patterns are deconvoluted through fitting as shown in Fig. 8. This linear discriminant mainly discriminates between healthy and damaged observations by the monoclinic fraction, the length of the orthorhombic a unit cell parameter and less so by peak broadening, although, the latter is to some degree correlated to the strain in unit-cell. Peak broadening seems, therefore, not to be dominated by unit-cell strain.

To investigate the robustness of this classification method against noisier data the signal-to-noise ratio was lowered by simulating and adding Gaussian noise. It was demonstrated that the noise could be increased by a factor of three while still maintaining a test classification accuracy of 100% using either 1D WAXS data or fitted parameters as input. The mean test classification accuracies of both methods are above 75% even when the noise is increased by a factor of 10.

The work presented in this paper demonstrates that WAXS and LDA can be used to distinguish between the binary classes of healthy and damaged UHMWPE ropes with very high accuracy. For practical usage it would be even more valuable to estimate the remaining life time of ropes. Therefore, further work should analyze a population of ropes from a more diverse set of conditions than healthy/damaged. Although the herein described method in principle can be helpful for defining a discard criteria, no attempt was made to do so here, for the damaged rope is a subjective attribute (no mechanical tests were performed) and no statistical evaluation over many ropes has been performed. We have preliminary data recorded on a SAXSLAB Ganesha on disassembled rope strands of approx. $7\,\text{mm}$ (data not shown) which underpins the generality of the approach presented here.

We suggest to average over multiple scans of a rope in proximity to each other since the information from a single scan is very localized and thus might not be representative for the overall section of the rope. We also suggest that WAXS could be used in combination with other probes to more accurately estimate the remaining life time by combining information from different length scales of the rope morphology. Future studies should also include parameters as the strain rate and effects like crystal aging as shown for UHMWPE applications elsewhere [37]. With regard to the fundamental understanding of the structural manifestation of the damage, SAXS could be further incorporated in the study design, although we believe that WAXS is more suitable to develop into a in-situ classification tool, because it is easier to acquire data (less space and time needed).

CRediT authorship contribution statement

Aksel S. Obdrup: Software, Formal analysis, Investigation, Data curation, Visualization, Writing – original draft. **D.C. Florian Wieland:** Investigation, Writing – review & editing. **Mathias K. Huss-Hansen:** Investigation. **Matthias M.L. Arras:** Conceptualization, Software, Data curation, Supervision, Project administration, Writing – review & editing. **Matti Knaapila:** Conceptualization, Supervision, Writing – review & editing, Funding acquisition.

Data availability

The raw data required to reproduce these findings cannot be shared at this time as the data also forms part of an ongoing study. The processed data required to reproduce these findings cannot be shared at this time due to legal or ethical reasons.

Acknowledgments

References

[1] P. Smith, P. Lemstra, Ultrahigh-strength polyethylene filaments by solution spinning/drawing, 2. Influence of solvent on the drawability, Makromolekul. Chem. 180 (12) (1979) 2983–2986, http://dx.doi.org/10.1002/macp.1979.021801220.

[2] P. Smith, P.J. Lemstra, Ultra-high-strength polyethylene filaments by solution spinning/drawing, J. Mater. Sci. 15 (2) (1980) 505–514, http://dx.doi.org/10.1007/BF02396802.

[3] P. Smith, P.J. Lemstra, Ultra-high strength polyethylene filaments by solution spinning/drawing. 3. Influence of drawing temperature, Polymer 21 (11) (1980) 1341–1343, http://dx.doi.org/10.1016/0032-3861(80)90205-0.

[4] P. Smith, P.J. Lemstra, J.P.L. Pijpers, A.M. Kiel, Ultra-drawing of high molecular weight polyethylene cast from solution, Colloid Polym. Sci. 259 (11) (1981) 1070–1080, http://dx.doi.org/10.1007/BF01524892.

[5] P. Smith, P.J. Lemstra, H.C. Booij, Ultradrawing of high-molecular-weight polyethylene cast from solution. II. Influence of initial polymer concentration, J. Polym. Sci. B: Polym. Phys. 19 (5) (1981) 877–888, http://dx.doi.org/10.1002/pol.1981.180190514.

[6] P. Smith, P. Lemstra, J. Pijpers, A. Kiel, Ultra-drawing of high molecular weight polyethylene cast from solution. III. Morphology and structure, Colloid Polym. Sci. 259 (11) (1981) 1070–1080, http://dx.doi.org/10.1007/BF01524892.

[7] M. Eijssen, Offshore wind farm construction: Easier, safer and more cost effective, in: International Conference on Offshore Mechanics and Arctic Engineering, in: Volume 5: Ocean Space Utilization; Ocean Renewable Energy, 2011, pp. 701–709, http://dx.doi.org/10.1115/OMAE2011-49847.

[8] M. Vlasblom, J. Boesten, S. Leite, P. Davies, Development of HMPE fiber for permanent deepwater offshore mooring, in: OTC Offshore Technology Conference, Vol. All Days, 2012, http://dx.doi.org/10.4043/23333-MS, OTC-23333-MS.

[9] O. Gronau, S. Belitskij, V. Sukhorukov, NDT of steel ropes with magnetic flaw detectors: documentation and interpretation of test result, Kontrol. Diagn. 9 (2000) 9–13, URL http://www.ndt.net/?id=774.

[10] ISO Central Secretary, Fibre Ropes for Offshore Stationkeeping : High Modulus Polyethylene (HMPE), Technical Report, ISO (International Organization for Standardization), Geneva, Switzerland, 2012.

[11] DNVGL (Det Norske Veritas & Germanischer Lloyd), Offshore Standard- Offshore Fibre Ropes, Technical Report, DNVGL Central Secretary, Oslo, Norway, 2015.

[12] R. Schlanbusch, E. Oland, E. Bechhoefer, Condition monitoring technologies for synthetic fiber ropes - a review, Int. J. Progn. Health Manag. 8 (2) (2017) http://dx.doi.org/10.36001/ijphm.2017.v8i2.2619.

[13] C.W. Bunn, The crystal structure of long-chain normal paraffin hydrocarbons. The "shape" of the< CH2 group, J. Chem. Soc. Faraday Trans. 35 (1939) 482–491, http://dx.doi.org/10.1039/TF9393500482.

[14] T. Seto, T. Hara, K. Tanaka, Phase transformation and deformation processes in oriented polyethylene, Japan. J. Appl. Phys. 7 (1) (1968) 31, http://dx.doi.org/10.1143/JJAP.7.31.

[15] K. Russell, B. Hunter, R. Heyding, Monoclinic polyethylene revisited, Polymer 38 (6) (1997) 1409–1414, http://dx.doi.org/10.1016/S0032-3861(96)00643-X.

[16] M.N. Collins, E. Dalton, B. Schaller, J. Leahy, C. Birkinshaw, Crystal morphology of strained ultra high molecular weight polyethylenes, Polym. Test. 31 (5) (2012) 629–637, http://dx.doi.org/10.1016/j.polymertesting.2012.03.009.

[17] E. Dalton, M.N. Collins, Lamella alignment ratio: a SAXS analysis technique for macromolecules, J. Appl. Crystallogr. 47 (3) (2014) 847–851, http://dx.doi.org/10.1107/S1600576714005706.

[18] L. Balzano, B. Coussens, T. Engels, F. Oosterlinck, M. Vlasblom, H. van der Werff, D. Lellinger, Multiscale structure and microscopic deformation mechanisms of gel-spun ultrahigh-molecular-weight polyethylene fibers, Macromolecules 52 (14) (2019) 5207–5216, http://dx.doi.org/10.1021/acs.macromol.9b00247.

[19] D. Istrate, G. van den Poel, M. Meuwissen, P. Smeets, H. Schneiders, P. Meessen, B. Tabor, X. Amils, M. Vierstraete, New approaches for studying UHMW-PE thermal behavior, 2006, URL https://vdocuments.site/new-approaches-for-studying-uhmw-pe-thermal-behavior-new-approaches-for-studying.html.

[20] J.B. Butcher, C. Day, J. Austin, P. Haycock, D. Verstraeten, B. Schrauwen, Defect detection in reinforced concrete using random neural architectures, Comput-Aided Civ. Inf. 29 (3) (2014) 191–207, http://dx.doi.org/10.1111/mice.12039.

[21] K. Jang, N. Kim, Y.-K. An, Deep learning–based autonomous concrete crack evaluation through hybrid image scanning, Struct. Health Monit. 18 (5–6) (2019) 1722–1737, http://dx.doi.org/10.1177/1475921718821719.

[22] M. Doaei, M.S. Tavallali, H. Nejati, Fault classification in electrofusion polyethylene joints by combined machine learning, thermal pulsing and IR thermography methods - A comparative study, Infrared Phys. Technol. 96 (2019) 262–266, http://dx.doi.org/10.1016/j.infrared.2018.11.032.

[23] M. Hiles, M. Grossutti, J. R. Dutcher, Classifying formulations of crosslinked polyethylene pipe by applying machine-learning concepts to infrared spectra, J. Polym. Sci. B: Polym. Phys. 57 (2019) 1255–1262, http://dx.doi.org/10.1002/polb.24837.

[24] S. Falconer, E. Nordgård-Hansen, G. Grasmo, Computer vision and thermal monitoring of HMPE fibre rope condition during CBOS testing, Appl. Ocean Res. 102 (2020) 102248, http://dx.doi.org/10.1016/j.apor.2020.102248.

[25] M. Khanmohammadi, A.B. Garmarudi, S. Samani, K. Ghasemi, A. Ashuri, Application of linear discriminant analysis and attenuated total reflectance Fourier transform infrared microspectroscopy for diagnosis of colon cancer, Pathol. Oncol. Res. 17 (2011) 435–441, http://dx.doi.org/10.1007/s12253-010-9326-y.

[26] M. Khanmohammadi, A.B. Garmarudi, M. de la Guardia, Feature selection strategies for quality screening of diesel samples by infrared spectrometry and linear discriminant analysis, Talanta 104 (2013) 128–134, http://dx.doi.org/10.1016/j.talanta.2012.11.032.

[27] C.J. Telford, B.A. Burrows, G. Sauzier, W. van Bronswijk, M.M. Houck, M. Maric, S.W. Lewis, Classification of polyethylene cling films by attenuated total reflectance-Fourier transform infrared spectroscopy and chemometrics, Anal. Methods 9 (2) (2017) 192–197, http://dx.doi.org/10.1039/C6AY02960D.

[28] W. Huang, K. Seehafer, U.H. Bunz, Discrimination of flavonoids by a hypothesis free sensor array, ACS Appl. Polym. Mater. 1 (6) (2019) 1301–1307, http://dx.doi.org/10.1021/acsapm.9b00116.

[29] X. Liang, M. Trentle, V. Kozlovskaya, E. Kharlampieva, M. Bonizzoni, Carbohydrate sensing using water-soluble poly (methacrylic acid)-co-3-(acrylamido) phenylboronic acid copolymer, ACS Appl. Polym. Mater. 1 (6) (2019) 1341–1349, http://dx.doi.org/10.1021/acsapm.9b00141.

[30] J. Kieffer, D. Karkoulis, Pyfai, a versatile library for azimuthal regrouping, J. Phys. Conf. Ser. 425 (20) (2013) 202012, http://dx.doi.org/10.1088/1742-6596/425/20/202012.

[31] M. Newville, T. Stensitzki, D.B. Allen, A. Ingargiola, LMFIT: Non-Linear Least-Square Minimization and Curve-Fitting for Python, Zenodo, 2014, http://dx.doi.org/10.5281/zenodo.11813.

[32] M. Otto, Chemometrics: Statistics and Computer Application in Analytical Chemistry, John Wiley & Sons, 2016.

[33] R.A. Fisher, The use of multiple measurements in taxonomic problems, Ann. Eugen. 7 (2) (1936) 179–188, http://dx.doi.org/10.1111/j.1469-1809.1936.tb02137.x.

[34] O. Ledoit, M. Wolf, A well-conditioned estimator for large-dimensional covariance matrices, J. Multivariate Anal. 88 (2) (2004) 365–411, http://dx.doi.org/10.1016/S0047-259X(03)00096-4.

[35] F. Pedregosa, G. Varoquaux, A. Gramfort, V. Michel, B. Thirion, O. Grisel, M. Blondel, P. Prettenhofer, R. Weiss, V. Dubourg, J. Vanderplas, A. Passos, D. Cournapeau, M. Brucher, M. Perrot, E. Duchesnay, Scikit-learn: Machine learning in python, J. Mach. Learn. Res. 12 (2011) 2825–2830, URL http://jmlr.org/papers/v12/pedregosa11a.html.

[36] A. Savitzky, M.J. Golay, Smoothing and differentiation of data by simplified least squares procedures., Anal. Chem. 36 (8) (1964) 1627–1639, http://dx.doi.org/10.1021/ac60214a047.

[37] M.N. Collins, E. Dalton, J.J. Leahy, C. Birkinshaw, Effects of tensile strain on the nanostructure of irradiated and thermally stabilised ultra high molecular weight polyethylenes for orthopaedic devices, RSC Adv. 3 (2013) 1995–2007, http://dx.doi.org/10.1039/C2RA21722H.